Estimates of C_n^2 from Numerical Weather Prediction Model Output and Comparison with Thermosonde Data

ROD FREHLICH, ROBERT SHARMAN, FRANCOIS VANDENBERGHE, WEI YU, YUBAO LIU, AND JASON KNIEVEL

National Center for Atmospheric Research, Boulder, Colorado*

GEORGE JUMPER

Battlespace Environment Division, Air Force Research Laboratory, Hanscom Air Force Base, Massachusetts

(Manuscript received 21 July 2009, in final form 23 March 2010)

ABSTRACT

Area-averaged estimates of C_n^2 from high-resolution numerical weather prediction (NWP) model output are produced from local estimates of the spatial structure functions of refractive index with corrections for the inherent smoothing and filtering effects of the underlying NWP model. The key assumptions are the existence of a *universal* statistical description of small-scale turbulence and a locally *universal* spatial filter for the NWP model variables. Under these assumptions, spatial structure functions of the NWP model variables can be related to the structure functions of the atmospheric variables and extended to the smaller underresolved scales. The shape of the universal spatial filter is determined by comparisons of model structure functions with the climatological spatial structure function determined from an archive of aircraft data collected in the upper troposphere and lower stratosphere. This method of computing C_n^2 has an important advantage over more traditional methods that are based on vertical differences because the structure function–based estimates avoid reference to the turbulence outer length scale. To evaluate the technique, NWP model–derived structure-function estimates of C_n^2 are compared with *nighttime* profiles of C_n^2 derived from temperature structure-function sensors attached to a rawinsonde (thermosonde) near Holloman Air Force Base in the United States.

1. Introduction

Forecasts of small-scale turbulence are important for aviation safety, communication reliability, optical imaging systems, GPS performance, and many other related problems. Past forecasts have been based on local vertical differences and the connection of the turbulence statistics to various theoretical scaling laws. Recent theoretical and experimental results for stably stratified anisotropic turbulence in the free atmosphere (Lindborg 1999, 2006; Cho et al. 1999; Cho and Lindborg 2001; Riley and Lindborg 2008) have shown that the horizontal turbulent eddies have a downscale cascade from the largest energy-containing scales to the smallest scales and that the turbulent statistics satisfy simple scaling laws. Similar results have been produced for the boundary layer with long flight tracks from research aircraft (Lenschow and Sun 2007). Current high-resolution numerical weather prediction (NWP) models can resolve the horizontal spatial scales of inhomogeneities that are connected by these simple scaling laws to the small-scale statistics of interest such as the energy dissipation rate ε for the velocity field and the structure constant C_T^2 for the temperature field. For optical and infrared wavelengths, the refractive index structure constant C_n^2 is related to C_T^2. For radio wavelengths the humidity field is also required to produce an estimate of C_n^2.

Starting from first principles, the horizontal spatial statistics of a random variable $u(\mathbf{x}, z)$ can be described by the second-order structure function [Tatarski 1967, his Eq. (3.14)]

$$D_u(\mathbf{s}, z) = \langle [u(\mathbf{x}, z) - u(\mathbf{x} + \mathbf{s}, z)]^2 \rangle, \qquad (1.1)$$

* The National Center for Atmospheric Research is sponsored by the National Science Foundation.

Corresponding author address: Dr. Rod Frehlich, NCAR/RAL, P. O. Box 3000, Boulder, CO 80307–3000.
E-mail: frehlich@ucar.edu

DOI: 10.1175/2010JAMC2350.1

where $\mathbf{x} = (x, y)$ is the horizontal spatial vector, z is the altitude, $\mathbf{s} = (s_x, s_y)$ denotes the horizontal displacement vector, and angle brackets denote an ensemble average. For small horizontal displacements [Tatarski 1967, his Eq. (3.18)],

$$D_u(\mathbf{s}, z) = C_u^2 s^{2/3}, \tag{1.2}$$

where C_u^2 is the structure constant for variable u (C_n^2 for refractive index n or C_T^2 for temperature T).

For most experiments using optical devices, or any other application that may be sensitive to scintillation effects caused by fluctuations in the atmospheric refractive index, a method for forecasting the scintillation levels would be highly desirable since that information could be used to modify the timing of an experiment, or even to cancel it. This obviously requires a forecast model of atmospheric conditions as a starting point. However, since most NWP models cover a fairly large area, the grid spacing of even high-resolution models is necessarily coarse [$\sim O$(1 km) horizontally and O(100 m) vertically] relative to the scales of scintillation [O(cm)]. Further, most NWP models suffer from inherent smoothing and filtering effects so that the smallest scales produced by the model are in fact underresolved (Frehlich and Sharman 2004, 2008; Skamarock 2004; Ferziger and Perić 2002). Therefore, assuming a downscale cascade from scales that are properly resolved by the model to the smallest scales of interest, estimates of small-scale turbulence statistics can be produced by applying corrections for this filtering. A model for the downscale cascade process for both the horizontal velocity and temperature in the upper troposphere and lower stratosphere has been provided in a recent series of papers by Lindborg (1999, 2006), Cho and Lindborg (2001), and Riley and Lindborg (2008). They showed that a simple power-law spectrum or structure function was valid for spatial scales from tens of kilometers to meter scales for both velocity and temperature. Frehlich and Sharman (2004) used these results to produce local estimates of velocity and temperature turbulence produced from structure functions of the NWP model output fields with a correction for the spatial filtering inherent in the NWP model. This algorithm was shown to produce unbiased estimates of turbulence statistics, such as ε, C_T^2, and C_n^2. However, the algorithm could only be evaluated for the upper troposphere and lower stratosphere because it was based on the in-cruise aircraft data used by Lindborg (1999). To extend this method to lower altitudes requires another source of data for comparison.

One source of temperature turbulence data over a wider range of elevations (from near the surface to typically 30-km elevation) is provided by ascents of the balloonborne thermosonde (Bufton 1975), which measures temperature turbulence from temperature differences across a 1-m horizontal rod attached to the top of the rawinsonde package. These temperature differences produce estimates of the second-order temperature structure function as well as C_T^2 using standard scaling laws within the inertial subrange.

In this paper we use a high-resolution multinested version of the Weather Research and Forecasting (WRF) NWP model (Skamarock et al. 2008) to produce forecasts of temperature that are used to compute structure functions of temperature and estimates of C_T^2 and C_n^2. This approach of using *horizontal* structure functions to estimate C_n^2 is in contrast to all previously published methods in which *vertical* differences of model state variables were used (Dewan et al. 1993; Cherubini et al. 2008). The resulting model predictions of C_n^2 using both the structure-function technique and a representative vertical differencing technique will be compared with thermosonde data for similar space–time observation periods. The structure function–based algorithm is introduced in section 2. Thermosonde measurements and WRF model runs are presented, respectively, in sections 3 and 4. Comparisons are given in section 5 followed by a summary and discussion in section 6.

2. Background

Small-scale turbulence can lead to strong fluctuations in the temperature and humidity and therefore the index of refraction n. For radio wavelengths, the refractive index $n(x, y, z)$ can be expressed in terms of the atmospheric temperature, pressure, and humidity, such as [Doviak and Zrnić 1993, their Eq. (2.19)]

$$n - 1 = 77.6 \times 10^{-6} \frac{P}{T} + 0.3733 \frac{e}{T^2}, \tag{2.1}$$

where P is the atmospheric pressure (hPa), T is atmospheric temperature (K), and e is water vapor partial pressure (hPa). For visible wavelengths a similar expression holds but is wavelength dependent (Goody 1964, appendix 4):

$$n - 1 = 0.284\ 198 \times 10^{-6} \frac{N_0 P[1 + 7.500\ 62 \times 10^{-7} P(5.337 - 0.0157T)]}{T}, \quad \text{wherein} \tag{2.2a}$$

$$N_0 = 64.328 + 29\,498.1/(146 - 1/\lambda^2) + 255.4/(41 - 1/\lambda^2) \quad (2.2b)$$

and λ is the wavelength (μm). For an (optical) wavelength of 0.5 μm,

$$n - 1 = \frac{79.281\,06 \times 10^{-6} P[1 + 7.500\,62 \times 10^{-7} P(5.337 - 0.0157T)]}{T}, \quad (2.3)$$

which is sometimes approximated as $(n - 1) = 79 \times 10^{-6}P/T$. These formulas connect C_n^2 to C_T^2 based on the local mean pressure P (hPa) and temperature T (K) by taking the derivative of Eq. (2.3)—that is (units: $m^{-2/3}$),

$$C_n^2 = (\partial n/\partial T)^2 C_T^2. \quad (2.4)$$

For visible radiation at $\lambda = 0.5$ μm, using Eq. (2.3),

$$C_n^2 = \left[\frac{79.281P(1 + 4.003\,08 \times 10^{-6}P) \times 10^{-6}}{T^2}\right]^2 C_T^2, \quad (2.5a)$$

which is approximated by

$$C_n^2 = (79 \times 10^{-6}P/T^2)^2 C_T^2. \quad (2.5b)$$

a. Vertical gradient approach

Early work produced estimates of C_n^2 assuming locally homogeneous and isotropic turbulence and a scaling law based on the vertical temperature or potential temperature gradient and an outer scale L_o that defines the typical size of the three-dimensional turbulent eddies. Then [Tatarski 1967, his Eq. (3.51)]

$$C_n^2 = a^2 M^2 L_o^{4/3}, \quad (2.6)$$

where a is a constant ($a^2 \approx 2.8$), the gradient of potential refractive index

$$M = 78.6 \times 10^{-6} \frac{P}{T^2} \frac{\partial \theta}{\partial z}, \quad (2.7)$$

and θ is the potential temperature.

The major difficulty in applying Eqs. (2.6) and (2.7) to compute C_n^2 from soundings or NWP model output is the lack of a rigorous basis for the computation of the outer length scale L_o Therefore, L_o is typically prescribed by some empirical function that relates it to stability and vertical wind shear (Hufnagel 1978; van Zandt et al. 1981; Dewan et al. 1993; Masciadri et al. 1999; Mahalov and Moustaoui 2010). For example, the Air Force Geophysics Laboratory (AFGL) model proposed by Dewan et al. (1993) uses

$$C_n^2 = 2.8M^2(0.1)^{4/3}10^Y \quad (2.8)$$

with two different empirical relationships for the troposphere and stratosphere,

$$Y = 1.64 + 42.0S \text{ Troposphere} \quad \text{and} \quad (2.9a)$$

$$Y = 0.506 + 50.0S \text{ Stratosphere}, \quad (2.9b)$$

where

$$S = \left[\left(\frac{du}{dz}\right)^2 + \left(\frac{dv}{dz}\right)^2\right]^{1/2} \quad (2.10)$$

is the magnitude of the vertical gradient of the horizontal velocity. In Eq. (2.10) S is limited to a maximum value of 0.045 s^{-1}, and $\partial T/\partial z$ implicit in M in Eq. (2.8) is limited to a maximum value of 10^{-6} K m^{-1}. Dewan et al. (1993) compared this model with the earlier models of van Zandt et al. (1981) and Hufnagel (1978) referenced above and with thermosonde data, with the Dewan et al. (1993) model showing better agreement. Therefore the Dewan et al. (1993) model will be compared with the structure-function approach outlined below. However, this model is based on high-resolution (~300 m vertically) rawinsonde measurements and shear/turbulence observations of rocket trails and may perform differently when applied to lower-resolution numerical model output. Note that modifications to the basic formulation have been proposed to improve the estimates of L_o for different stability regimes and model parameterizations (Masciadri et al. 1999; Mahalov and Moustaoui 2010), but in practice they require very high vertical resolution for actual implementation.

b. Structure-function approach

Following Lindborg (1999) and Cho and Lindborg (2001), we assume the temperature and velocity structure functions follow simple scaling laws for homogeneous turbulence in the horizontal plane at a fixed altitude or pressure level. Since the WRF model is run at high resolution, we assume the functional form of Lindborg (1999) is valid at small spacing s; that is,

$$D_T(s) = a_1 s^{2/3} + b_1 s^2 - c_1 s^2 \ln s, \quad (2.11)$$

where b_1 and c_1 are constants and $a_1 = C_T^2$, since at the smallest spacing $D_T(s) = C_T^2 s^{2/3}$ [Eq. (1.2)]. This form is based on comparisons with specially instrumented commercial aircraft data from the Global Atmospheric Sampling Program (Nastrom and Gage 1985) campaign in the United States and Measurements of Ozone by Airbus In-Service Aircraft (MOZAIC) in Europe (Lindborg 1999; Cho and Lindborg 2001). Both of these campaigns used commercial aircraft, and hence measurements are concentrated in the upper troposphere and lower stratosphere. However, a similar universal description has also been observed at lower altitudes (Lenschow and Sun 2007) and in the stratosphere (Cho et al. 1999).

The constants in Eq. (2.11) were determined for the temperature structure function $D_T(s)$ by Frehlich and Sharman (2004) assuming that the temperature spectrum from Fig. 5 of Nastrom and Gage (1985) has the same shape as the velocity spectrum. This is a good approximation for spatial scales of less than 100 km for which the first term in Eq. (2.11) dominates. These are (for D_T in units of kelvins squared and s in units of meters)

$$\begin{aligned} a_1 &= 6.36 \times 10^{-4}\ \mathrm{K^2\ m^{-2/3}}, \\ b_1 &= 4.24 \times 10^{-10}\ \mathrm{K^2\ m^{-2}}, \quad \text{and} \\ c_1 &= 2.83 \times 10^{-11}\ \mathrm{K^2\ m^{-2}}. \end{aligned} \tag{2.12}$$

In practice, as shown by Frehlich and Sharman (2004), Eq. (2.11) requires modifications to account for NWP model specific finite differencing, smoothing, and model parameterization effects. These effects can be estimated as described below.

In an NWP model it is common practice to represent the desired discrete model variables (''truth'') as a spatial average of the random atmospheric fields centered in a model grid cell (e.g., Daley 1993):

$$v_{\mathrm{truth}}(\mathbf{r}) = \int_{-\infty}^{\infty}\int_{-\infty}^{\infty}\int_{-\infty}^{\infty} W(\mathbf{r}-\mathbf{s})v(\mathbf{s})\, d\mathbf{s}, \tag{2.13}$$

where $\mathbf{r} = (x, y, z)$ denotes the center of the grid cell, $W(\mathbf{s})$ is the effective weighting function [filter function with normalization $\int\int\int W(\mathbf{s})\, d\mathbf{s} = 1$] of the model and $d\mathbf{s}$ denotes 3D integration.

For a homogeneous field, the local horizontal spatial statistics of a model output variable $\tilde{u}$ are also described by the spatial structure function defined by

$$D_{\tilde{u}}(s_x, s_y, z) = \langle [\tilde{u}(x, y, z) - \tilde{u}(x + s_x, y + s_y, z)]^2 \rangle. \tag{2.14}$$

Assume the model values $\tilde{u}$ are given by the general form Eq. (2.13) and the filter function $W(r)$ is a universal function. In practice, the filter function may also depend on conditions such as the local stability and the subgrid parameterization. We assume that this is a weak dependence and only the average form of $W(r)$ is required for the estimates of C_n^2. Then unbiased estimates of the local structure function in the (x, y) plane of $\tilde{u}$ for a small region centered at coordinate $(x, y, z) = (iL_x, jL_y, H)$ is given by

$$D_{\tilde{u}}(\ell L_x, mL_y, H) = \frac{1}{(2N_i - \ell + 1)(2N_j - m + 1)} \sum_{p=i-N_i}^{i+N_i-\ell} \sum_{q=j-N_j}^{j+N_j-m} [\tilde{u}(p, q, H) - \tilde{u}(p + \ell, q + m, H)]^2, \tag{2.15}$$

where H denotes the altitude of the model grid cell and N_i and N_j define the domain in the x and y directions, respectively. The size of the measurement domain is determined by the required statistical accuracy and the effective resolution of the estimates of C_n^2. The model structure function is a filtered version of the actual structure function of the continuous random process for variable u because of the spatial filter of the model.

The ensemble average of the model structure function is given by (Papoulis 1965)

$$\begin{aligned} D_{\mathrm{model}}(\mathrm{s}) = \langle D_{\tilde{u}}(\mathbf{s}) \rangle &= \int_{\infty}^{\infty} D_u(\mathbf{r}) V(\mathbf{s}-\mathbf{r})\, d\mathbf{r} \\ &\quad - \int_{\infty}^{\infty} D_u(\mathbf{r}) V(-\mathbf{r})\, d\mathbf{r}, \end{aligned} \tag{2.16}$$

where

$$V(\mathbf{s}) = \int_{\infty}^{\infty} W(\mathbf{s}-\mathbf{r}) W(\mathbf{r})\, d\mathbf{r} \tag{2.17}$$

is the autocorrelation of the filter function W. An empirical function $D_{\mathrm{model}}(s)$ for the model-derived structure functions can be written as (Frehlich and Sharman 2004)

$$D_{\mathrm{model}}(s) = K D_{\mathrm{cor}}(s) D_{\mathrm{ref}}(s), \tag{2.18}$$

where K is a constant, $D_{\mathrm{cor}}(s)$ describes the correction to account for underrepresentation of the smaller scales produced by the NWP model filter, and $D_{\mathrm{ref}}(s)$ is a normalized form of the best-fit structure functions derived by Lindborg (1999), [Eq. (2.11)]; that is,

$$D_{\text{ref}}(s) = s^{2/3} + \frac{b_1}{a_1}s^2 - \frac{c_1}{a_1}s^2 \ln s. \tag{2.19}$$

The correction function $D_{\text{cor}}(s)$ should approach unity for large separations where the effects of the spatial filter are negligible. For small spacing s, the model structure function $D_{\text{model}}(s)$ should approach s^2 to reflect the spatial smoothing of the fields at the smallest scales. An empirical function that satisfies both these requirements is (Frehlich and Sharman 2004)

$$D_{\text{cor}}(s) = \frac{(s/p_1)^{4/3}}{1 + (s/p_1)^{4/3} + p_2(s/p_1)^{2/3}}, \tag{2.20}$$

where p_1 is the length scale of the NWP model-specific filter and p_2 is a fitting parameter. These parameters are determined in section 5. The best fit of the model-derived structure function and the empirical model $D_{\text{model}}(s)$ of Eq. (2.18) produces an estimate of the constant K by minimizing the χ^2 error defined by

$$\chi^2 = \sum_{k=1}^{N} \frac{[D_{\tilde{u}}(s_k) - D_{\text{model}}(s_k)]^2}{\text{Var}[D_{\tilde{u}}(s_k)]} = \sum_{k=1}^{N} \frac{[D_{\tilde{u}}(s_k) - D_{\text{model}}(s_k)]^2}{kD^2_{\text{model}}(s_k)}, \tag{2.21}$$

where s_k denotes the separation distance at lag k, and the variance of the estimates $\text{Var}[D_{\tilde{u}}(s_k)]$ is approximated by $kD^2_{\text{model}}(s_k)$ assuming χ^2 statistics, that is, the temperature differences are independent zero-mean Gaussian random variables. The value of K in (2.18) that minimizes the χ^2 error is given by

$$K = \frac{\sum_{k=1}^{N} \dfrac{D^2_{\tilde{u}}(s_k)}{kD^2_{\text{cor}}(s_k)D^2_{\text{ref}}(s_k)}}{\sum_{k=1}^{N} \dfrac{D_{\tilde{u}}(s_k)}{kD_{\text{cor}}(s_k)D_{\text{ref}}(s_k)}}. \tag{2.22}$$

If the variable u is temperature, the best-fit value of K is the estimate of C_T^2, which is converted to an estimate of C_n^2 using Eq. (2.5b).

The structure-function estimates of C_n^2 are calculated at each NWP grid point (x, y, η) for the full model domain except near the edges. Since the WRF model uses a terrain-following vertical coordinate η, the temperature or refractivity structure functions are calculated at each grid point on a constant geometric altitude z by interpolating the surrounding variables T to the same altitude z. Calculations on constant-altitude surfaces greatly reduce the spurious contributions that are produced by calculations in the terrain-following coordinates, especially in the vicinity of complex terrain. The linear interpolation over these small distances is a good approximation since the structure functions have an s^2 dependence over these spatial separations, which implies linear spatial dependence of the variables. In this formulation, no estimate of C_n^2 is produced near the surface if any neighboring temperature field at height z is below the surface.

To summarize the procedure, estimates of C_n^2 from WRF output are produced by the following sequence of steps:

1) Determine the coefficients p_1 and p_2 of Eq. (2.20) for the WRF model filtering assuming a universal shape of the structure functions and model filter (see section 5).
2) Calculate the average temperature structure function in the east–west and north–south directions at the model grid point (l, m, H) by interpolating neighboring values to the same altitude H using Eq. (2.15).
3) Determine the best-fit constant $K = C_T^2$ by minimizing the χ^2 error between the theoretical model and the average structure function using Eq. (2.22).
4) Convert the estimate of C_T^2 to C_n^2 using Eq. (2.5b).

These WRF model-derived structure-function estimates of C_n^2 for visible wavelengths (no humidity component) are compared with the collocated thermosonde profiles in section 5.

3. Thermosonde data

The truth data used in this study are vertical profiles of wind, temperature, humidity, and C_T^2 measured by thermosonde balloons during a field campaign in 2004 at Holloman Air Force Base (AFB) in New Mexico. After initial NASA development, the thermosonde has been used by the Air Force Research Laboratory to measure optical C_n^2 profiles. As mentioned above, the instrument is mounted on a standard meteorological rawinsonde carried by a balloon. Two fine-wire resistance temperature probes measure the temperature difference over a horizontal separation of 1 m. The squared temperature difference is then averaged over a 4-s time interval to estimate C_T^2, which is converted to C_n^2 with Eq. (2.5b).

The key assumption is that the local turbulence has an inertial range scaling of $s^{2/3}$ for a horizontal separation $s = 1$ m. The ascent rate of the thermosonde is between 5 and 7 m s^{-1}. Data are typically useful to an altitude of 30 km. The estimation error or standard deviation (SD) of C_T^2 and therefore C_n^2 is dominated by the spatial

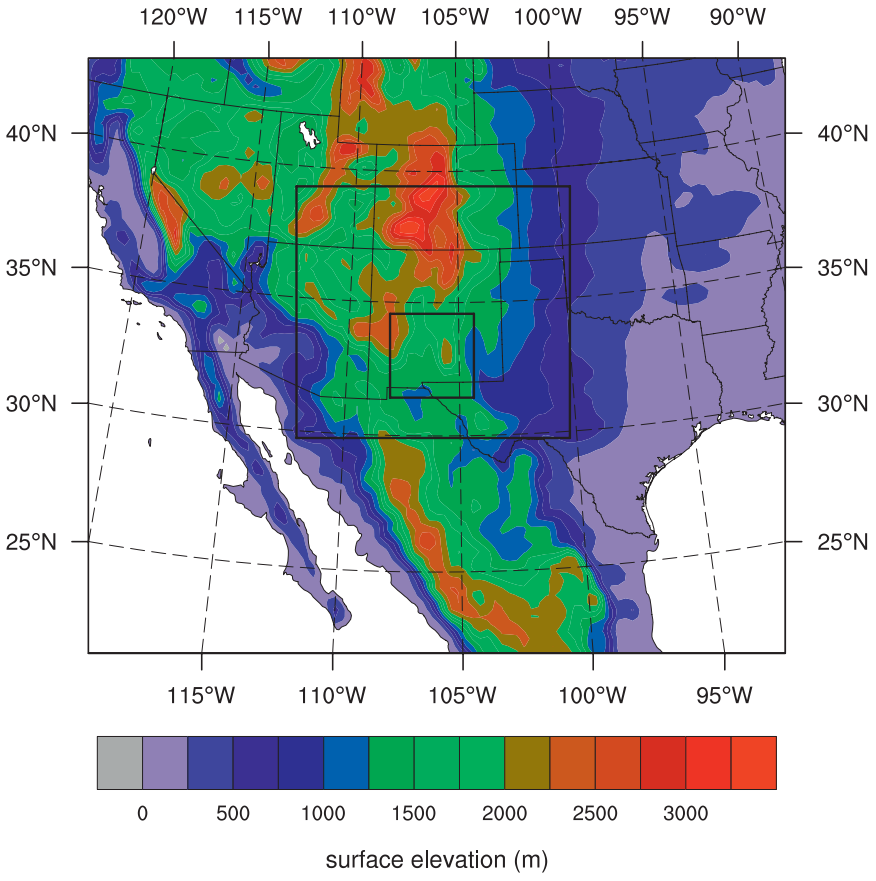

FIG. 1. Computational domain for the WRF model. The grid intervals are 30, 10, and 3.3 km, respectively, for domains 1 (D1), 2 (D2), and 3 (D3).

sampling of the random atmosphere. For a Gaussian random temperature field with homogeneous statistics over the measurement domain, the $\mathrm{SD}(C_T^2) = (1.331s/L)^{1/2}C_T^2$ [see Lenschow et al. 1994, their Eq. (32)], where s is the separation of the sensors (1 m), L is the vertical length of atmosphere sampled during the observation time by the thermosonde, and C_T^2 is the "true" value. For a rise rate of 5 m s^{-1} and a 4-s measurement time, $L = 20$ m and $\mathrm{SD}(C_T^2) = 0.2580C_T^2$; for an averaging interval of $L = 100$ m, $\mathrm{SD}(C_T^2) = 0.1331C_T^2$ (i.e., 13.3% of the true value).

4. WRF model setup

The WRF model, version 3.0.1.1 (Skamarock et al. 2008), was run over three nested grid domains with grid intervals of 30, 10, and 3.3 km, respectively. The configuration of the nested domains is illustrated in Fig. 1. A one-way nested approach is employed wherein each coarse domain provides boundary forcing to the finer domain it encompasses. The η model levels were defined using the default WRF assignment procedure for a model top of 10 hPa (~30 km) and 80 vertical levels. The physical parameterizations that were used are given in Table 1. Both the Mellor–Yamada–Janjić (MYJ) (Janjić 2002; Skamarock et al. 2008) and Yonsei University (YSU) (Hong et al. 2006; Skamarock et al. 2008) planetary boundary layer (PBL) parameterizations were used, and differences will be presented below.

To damp gravity waves reflected from the top boundary, the implicit Rayleigh damping scheme of Klemp

TABLE 1. WRF parameterization options used for the simulations (cf. Skamarock et al. 2008). Here, MM5 is the fifth-generation Pennsylvania State University–NCAR Mesoscale Model.

Physical process	Scheme
Cumulus (on 30-/10-km domains)	Grell–Devenyi ensemble scheme
Microphysics	Purdue Lin six-class scheme
Longwave radiation	Rapid Radiative Transfer Model
Shortwave radiation	MM5 (Dudhia)
Boundary layer	YSU, MYJ
Surface layer	MM5 with YSU, Eta with MYJ
Land surface	"Noah" land surface model

TABLE 2. Statistical analysis of difference in observed $\log C_n^2$ from the thermosonde and model predictions of C_n^2; angle brackets denote the ensemble average, and SD denotes standard deviation.

	$\langle \log(C_n^2)_{\text{obs}} - \log(C_n^2)_{\text{Model}} \rangle$		$\text{SD}[\log(C_n^2)_{\text{obs}} - \log(C_n^2)_{\text{Model}}]$	
Initialization time/PBL scheme	Model = WRF	Model = Dewan	Model = WRF	Model = Dewan
Troposphere				
12 MYJ	0.154	0.0707	0.555	1.281
12 YSU	0.121	0.0439	0.588	1.350
18 MYJ	0.135	0.0818	0.546	1.225
18 YSU	0.130	0.0625	0.578	1.239
Stratosphere				
12 MYJ	0.135	0.119	0.687	0.380
12 YSU	0.103	0.1072	0.625	0.382
18 MYJ	0.152	0.125	0.861	0.373
18 YSU	0.004 98	0.1108	0.8438	0.374

et al. (2008) was applied in the top 15 km of the model domain with a maximum damping coefficient of 0.2. Spurious noise, apparently related to steeply sloping terrain, was found in some model fields when the standard 30-arc-s values from the U.S. Geological Survey terrain were interpolated to the 3.3-km model grids. Most of the noise disappeared when we smoothed the model terrain with a nine-point, two-dimensional binomial filter. A detailed exploration of the noise is beyond the scope of this paper, but we suspect that it stems from the inconsistent numerical discretization of the horizontal gradient terms that can arise in terrain-following coordinate systems, as described by Mahrer (1984).

Initial conditions and lateral boundary conditions for the largest domain were provided by the 1° 0–24-h forecasts from the operational Global Forecast System (GFS) of the National Centers for Environmental Prediction, archived at the National Center for Atmospheric Research (NCAR). GFS data are publicly available in real time and are one of the datasets normally used to drive the WRF model for real-time applications. Although GFS analyses were available during this time period, because our simulations were retrospective we instead used only the analyses that coincided with the start times of each WRF model simulation. Updates to the WRF model lateral boundary conditions during each simulation were from GFS model forecasts interpolated in time from 6-h GFS model updates. This mimics what would be done in real-time applications.

For each case for which we had viable thermosonde data, we executed four WRF forecasts, one initialized at 1200 UTC and the other at 1800 UTC on the previous day, each using the MYJ and YSU PBL schemes. Since most of the thermosonde launches occurred between 0400 and 0600 UTC, these two sets of model runs provided forecast lead times of roughly 10–12 h for the initialization at 1800 UTC and 16–18 h for the initialization at 1200 UTC.

5. Comparison of WRF-model estimates of C_n^2 with thermosonde data with the AFGL model

The thermosonde data used for the comparisons are from a field campaign conducted at Holloman AFB on 13–21 July 2004. One or two launches were performed in the late evening on most of the days during this time, but some had missing or unreliable data so that only 10 profiles were actually useful for comparison. Because of the large random variations in the atmosphere that are due to the intermittent character of turbulence, different averaging domains, and limited number of profiles, reliable statistical evaluations of performance are difficult. However, standard statistical analyses for the 10 profiles were performed and are tabulated in Table 2 for the average difference and SD of the difference between the thermosonde estimates of $\log C_n^2$ (averaged over the corresponding WRF model vertical spacing, which varies from 200 to 300 m in the troposphere) and the model-based predictions of $\log C_n^2$ for the troposphere and stratosphere. Based on these statistical evaluations, the ''best case'' (0200 UTC 19 July 2004) and ''worst case'' (0400 UTC 16 July 2004) were selected for the MYJ model run initialized at 1800 UTC based on the SD of the differences. Profiles of the standard rawinsonde variables [wind speed and direction, temperature, and relative humidity (RH)] for the best and worst cases are shown in Figs. 2 and 3, respectively. Given the relatively long lead time of the model forecasts, the overall agreement between the modeled and observed profiles is fairly good for both cases, although the vertical resolution of the model is insufficient to capture the small-scale vertical structures in the soundings for either case. The presence of these observed small-scale features underscores the difficulty inherent in using

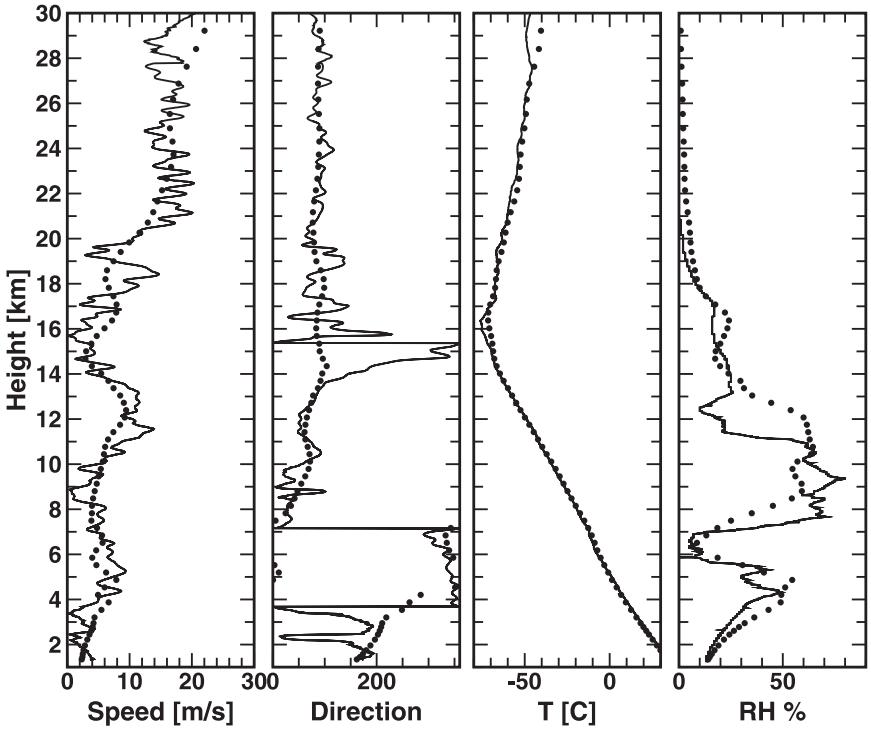

FIG. 2. Comparison of thermosonde data (solid line) with WRF/MYJ (dots) for the best case on 0200 UTC 19 Jul 2004.

vertical differencing of model variables to derive C_n^2. The most significant difference in the two profiles is the larger deviation in the modeled versus observed temperature near the tropopause in the worst case. There are also some differences in the profiles of RH. However, these differences should have little impact on estimates of C_n^2 since the thermosonde estimates are based solely on temperature. In these comparisons a balloon-drift tracking algorithm was employed to determine the nearest horizontal grid point using the modeled velocity vector and a constant rise rate of 5 m s^{-1}. Since most of the cases had light winds, the balloon trajectory was usually contained within three model grid points from the launch coordinate.

Model-derived estimates of the refractive index structure function $D_n(s)$ are produced from the temperature structure function $D_T(s)$ using Eq. (2.15) and the conversion factor of Eq. (2.5b). The correction for the WRF model effective spatial filter is defined by the parameters p_1 and p_2 of Eq. (2.20), which are determined from the average structure function at fixed altitudes for the WRF model forecasts produced over the 9-day period of the thermosonde data at an altitude range of 8–12 km [representative of the altitude range of the aircraft data from which the Lindborg reference model Eq. (2.19) was developed]. The average $D_T(s)$ for separations s in the west–east $[D_{Tx}(s)]$ and south–north $[D_{Ty}(s)]$ directions is shown in Fig. 4. The structure function $D_{Tx}(s)$ has slightly larger values for small separations, probably because of the presence of south–north-aligned mountain waves (Frehlich and Sharman 2008) produced by the local terrain. Therefore $D_{Ty}(s)$ is used to estimate the effective model filter $W(r)$ in Eq. (2.17). The parameters p_1 and p_2 of the best-fit model Eqs. (2.18)–(2.20) were determined by minimizing the χ^2 error Eq. (2.21) for all variables (p_1, p_2, K) using the Powell method (Press et al. 1986), yielding $p_1 = 6.621$ km and $p_2 = -0.538\,94$. This best-fit model is shown in Fig. 5 as well as the Lindborg reference model Eq. (2.11) and $D_{Ty}(s)$. Note that the large separations do not agree with the Lindborg model, which is probably because the short analysis period does not sample all of the large-scale processes observed over a full year.

The estimates of C_n^2 are produced from the best-fit parameter K [see Eqs. (2.18)–(2.22)] using the WRF model structure functions with a 5×5 gridpoint box at each model coordinate with the model values from the surrounding points interpolated to the same altitude. Examples of the structure-function estimates $D_n(s)$ and the best-fit model for a few different altitudes for flight 16 (0600 UTC July 19 2004) are shown in Fig. 6. The shapes of the structure functions are in good agreement

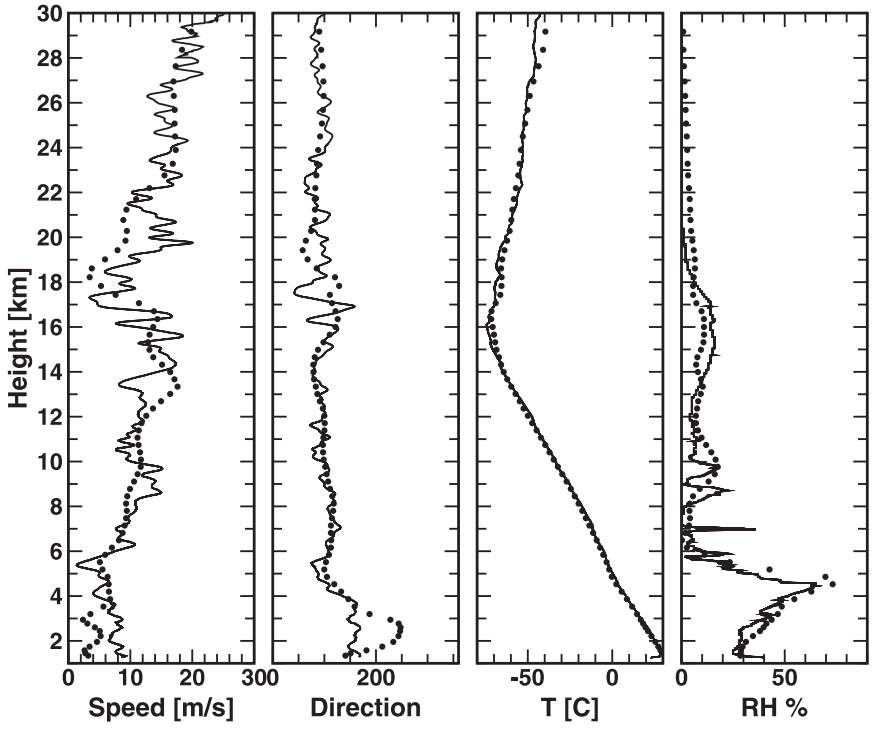

FIG. 3. As in Fig. 2, but for the worst case on 0400 UTC 16 Jul 2004.

with the theoretical model for all of the altitudes. It is interesting that the structure functions follow the predictions of the Lindborg model even at low altitudes. This may reflect the large-scale energy in boundary layer processes that have been observed in aircraft data and might be related to the influence of mesoscale processes (Lenschow and Sun 2007). Since the smallest lags s have the largest number of independent samples, they are the most accurate and therefore dominate the estimates of C_n^2 [see Eqs. (2.21) and (2.22)], as shown by the good agreement at the smallest lags in comparison with the largest lag.

A comparison of the C_n^2 profiles from two thermosonde launches separated by 1 h is shown in Fig. 7. The general features of the profiles are similar but there are large local variations, indicating the highly intermittent nature of the turbulent field, which is not captured by the area-averaged estimates of C_n^2 from the WRF model. The peak-to-peak variability of C_n^2 is approximately one order of magnitude, which implies an rms error of approximately 50%. Since the estimation error of C_n^2 for a 100-m altitude layer is approximately 13.3% (see above), the intrinsic intermittency of atmospheric turbulence dominates the error analysis.

The profiles of C_n^2 from the thermosonde are compared with estimates from the WRF model initialized at 1800 UTC in Figs. 8 and 9, corresponding to the best and worst cases, respectively. There is generally good agreement between the thermosonde data and the estimates of C_n^2 from the model, especially near the surface and between about 10- and 20-km elevation. Large spatial

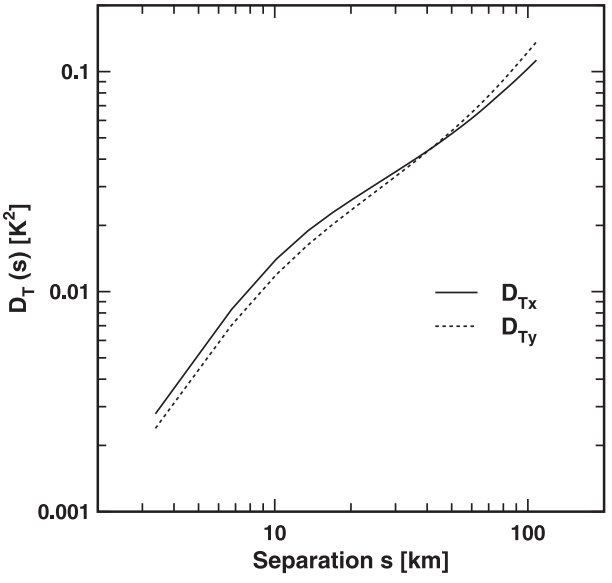

FIG. 4. Average temperature structure functions over the altitude range of 8–12 km for separation in the west–east direction (D_{Tx}; solid line) and the south–north direction (D_{Ty}; dotted line) for the period 13–21 Jul 2004.

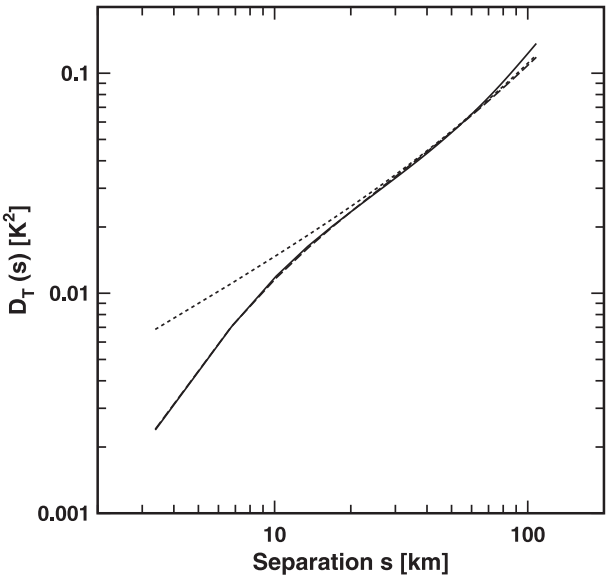

FIG. 5. Average temperature structure function D_{Ty} from the WRF model (solid line), best-fit model Eq. (2.18) (dashed line), and reference model Eq. (2.11) (dotted line).

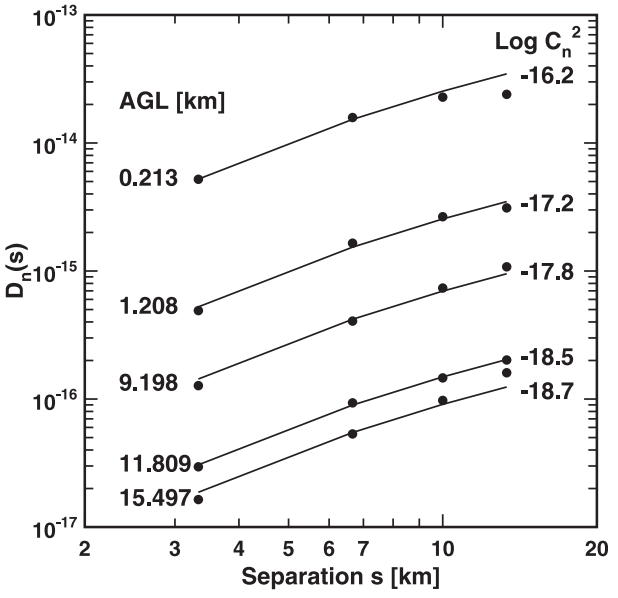

FIG. 6. Examples of structure-function estimates $D_n(s)$ from WRF output (dots) and the best-fit model (Eq. 2.18) (line) for various altitudes from the best-case run shown in Fig. 2.

variations in the thermosonde estimates are expected because of the intermittency of turbulence [see Fig. 7 and Frehlich et al. (2004)]. These variations cannot be represented by the large area averaging of the structure-function estimates from the WRF model. The fact that the structure function–based estimates produce good agreement with the thermosonde data near the surface is a surprising new result since scaling for the boundary layer is typically different from scaling for the free atmosphere. However, these are nighttime data, when the boundary layer is shallow, and so the WRF model might be able to resolve the relevant scales in the residual layer, which may be dominated by random larger-scale gravity waves. Reliable structure-function estimates of the area-averaged C_n^2 should be produced if the turbulence scaling laws are valid in the horizontal plane and if the WRF model correctly resolves the atmospheric statistics over the 5×5 gridbox averaging domain. In the upper part of the model domain, the WRF model configuration uses the Rayleigh damping option (Skamarock et al. 2008) in which the damping coefficient increases as $\sin^2(z)$ from the base of the damping layer at 15 km to the model top at 30 km. Since the damping coefficient has half its maximum value at about 22-km elevation, the smaller scales in the model profiles will generally be damped sufficiently to underestimate the observations above about 20 km, and the effect of this damping on C_n^2 profiles above this level is obvious in the figures. Note that a spectrum of gravity waves is generated by flow over the complex terrain in the model in the vicinity of Holloman AFB, with a dominant wavelength of about 40 km ($\sim 13\Delta x$), and these do contribute to the observed horizontal variability of temperature and other fields.

For reference, profiles of C_n^2 computed from the AFGL empirical model using the vertical difference formulation from the WRF output fields, Eq. (2.8), are

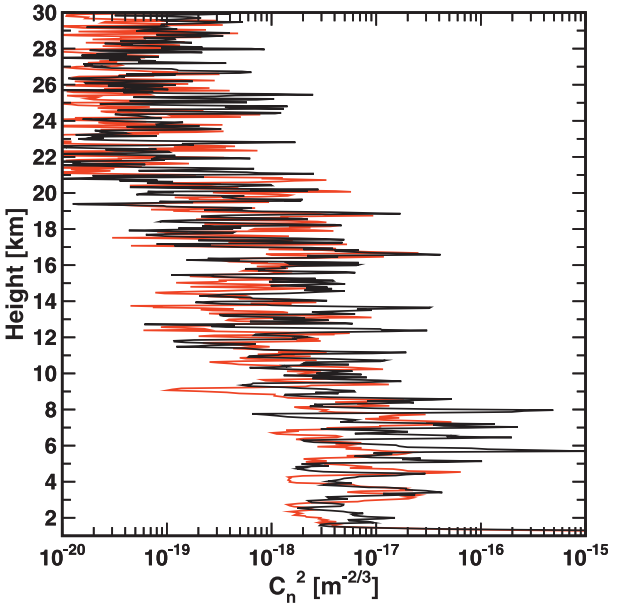

FIG. 7. Comparison of thermosonde profiles of C_n^2 with approximately 100-m vertical averaging separated by 1 h starting at 0200 UTC 19 Jul 2004.

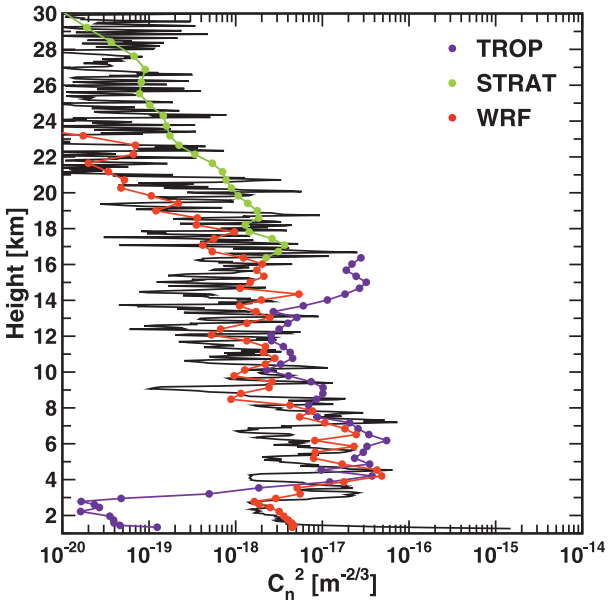

FIG. 8. Thermosonde profile of C_n^2 (black line) for the best case, WRF/MYJ structure-function estimates of C_n^2 for visible wavelengths (red line), and AFGL model predictions for the troposphere (TROP; blue line) and stratosphere (STRAT; green line) at 0200 UTC 19 Jul 2004.

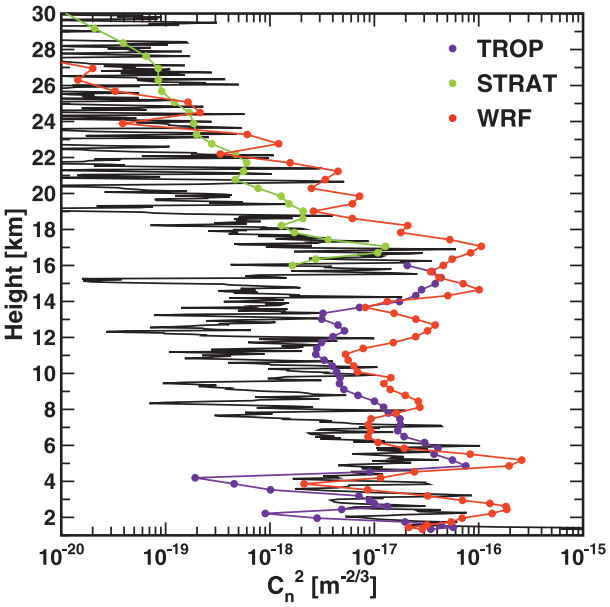

FIG. 9. As in Fig. 8, but for the worst case at 0400 UTC 16 Jul 2004.

also shown in Figs. 8 and 9. The stratospheric version, Eq. (2.9b), is used above the rawinsonde-inferred tropopause height of 16 km while the troposphere version, Eq. (2.9a), is used below it. These results are typical of the AFGL model results, which tend to underestimate C_n^2 in the lowest 4–5 km and to overestimate C_n^2 just below the tropopause. The stratospheric predictions of C_n^2 are typically in better agreement at the higher altitudes, but the tropospheric and stratospheric predictions rarely agree at the tropopause.

The profiles for the cases displayed in Figs. 8 and 9 are typical of the results for other cases, which is reflected in overall statistical data shown in Table 2, which separates the rms error of $\log C_n^2$ into two components: a bias component and the SD of the difference of $\log C_n^2$—that is, $\mathrm{RMSE}(\log C_n^2) = \{\langle[\log(C_n^2)_{\mathrm{obs}} - \log(C_n^2)_{\mathrm{model}}]\rangle^2 + \mathrm{SD}[\log(C_n^2)_{\mathrm{obs}} - \log(C_n^2)_{\mathrm{model}}]^2\}^{1/2}$. The results in Table 2 show that the SD is more consistent than the mean difference over the four sets of cases and dominates the error statistics, especially in the troposphere. Note that the mean differences are smaller than the SD of the differences, and therefore the statistical confidence in the mean is poor. Based on the SD of the differences, as expected, the initialization at 1800 UTC gives better results than the longer-lead forecasts initialized at 1200 UTC, and overall the MYJ seems to give better results. For the troposphere, the structure-function estimates perform better than the Dewan model. For the stratosphere, the Dewan model performs better and the error is generally larger than in the troposphere, but because of the sponge the comparison in the stratosphere has many fewer points than in the troposphere.

The spatial variability of C_n^2 is shown in Fig. 10 for the best case, at an altitude of 10 km. The large spatial variations of C_n^2 typically cover more than two orders of magnitude and are similar to the variations in the level of the temperature and velocity spectra determined from aircraft data (see Nastrom and Gage 1985, their Fig. 5) and from NWP model output (Frehlich and Sharman 2004, their Figs. 9 and 10).

6. Summary and discussion

The WRF model, version 3.0.1.1 (Skamarock et al. 2008), with initialization and boundary conditions provided by the GFS model was used to estimate C_n^2 for 9 days in July 2004 over the southwestern United States. The computational domain was 30 km deep and had a horizontal grid interval of 3.3 km with 80 vertical levels. The model output was compared with independent observations of wind, temperature, humidity, and C_n^2 taken from 10 high-resolution thermosonde profiles observed at night during a pair of field campaigns at Holloman AFB. Four forecasts were produced for each comparison by using two lead times (10–12 h and 16–18 h) and two PBL parameterization schemes. Despite the fairly long lead times and a computational domain that includes complex terrain, overall the WRF forecast model output compared

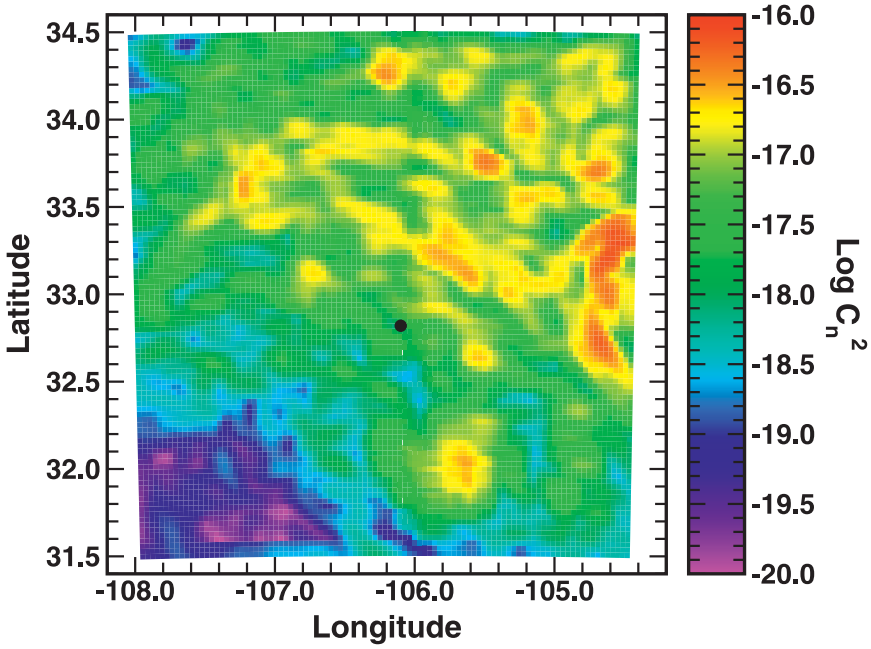

FIG. 10. Map of C_n^2 from WRF/MYJ for the best-case example at an altitude of 10 km at 0200 UTC 19 Jul 2004. The location of the thermosonde launch site is indicated by the black disk.

favorably to the observations, particularly in the lowest few kilometers.

An algorithm to estimate the area-averaged optical (visible) C_n^2 parameters from NWP model output was presented and applied to the forecast temperature fields from the WRF model. The algorithm has its basis in theoretical and experimental results connecting the larger-scale horizontal spatial statistics to the smallest scales (Lindborg 1999; Cho and Lindborg 2001; Riley and Lindborg 2008). The universal behavior of these results allows estimates of small-scale temperature (and velocity) turbulence from second-order structure functions computed from larger-scale NWP model output, provided corrections are made for NWP model-specific smoothing and filtering effects (Frehlich and Sharman 2004). This technique of using horizontal variability estimates from the NWP model output differs fundamentally from more traditional approaches to computing C_n^2, which rely on vertical differences. We think this is a more reliable approach given that the very finescale vertical structures in the atmosphere cannot be resolved with current operational mesoscale NWP models. It also eliminates the need to specify the outer length scale of the turbulence L_o, required by vertical difference formulations of C_n^2, which is difficult to estimate in stably stratified turbulence.

In general, the structure function–based estimates of C_n^2 agree fairly well with the thermosonde data, although, as expected, the thermosonde observations exhibit much more variability because of the much smaller measurement volume and the intermittency of turbulence (see Fig. 7). Note that the intrinsic spatial variability of C_n^2 is typically much larger than the estimation (instrument) error and therefore dominates the thermosonde errors. Since the structure-function estimates are based on the horizontal variability of the temperature field, they are sensitive to both WRF and GFS model errors. Overall, the best agreement with observations was obtained between 10 and 20 km above the ground, but the structure-function estimates in the lowest 10 km were also relatively good, given that the nighttime residual layer is a turbulent region that is very challenging for mesoscale models. Results above 20 km quickly degrade, partly because of the miscalculations of balloon drift, the mismatch of time (since the balloon took more than 1 h to reach 30-km altitude), and nonphysical small-amplitude gravity waves near the model top (these are obvious in cross-sectional plots, not shown), which although substantially damped still had amplitudes significant enough to affect the structure-function calculations. It was found that the C_n^2 values at all levels are sensitive to the PBL parameterization scheme used. This is due in part to the fact that the PBL scheme affects the magnitude of the horizontal and vertical velocities at the surface, which in turn modifies the upward forcing for gravity wave generation for a given terrain slope, especially for light winds and stable conditions. Although the results using structure

function–based C_n^2 estimates presented here are promising, only a small number of thermosonde profiles (10) were available for the statistical comparison.

In the near future, as NWP models are run at finer resolutions, phenomena that lead to the creation of gravity waves will be better resolved, resulting in more realistic representations of wave-generated turbulence, which should allow better predictions of small-scale turbulence and C_n^2, assuming the turbulence scaling laws (structure-function scaling) are valid for these random wave-generation regimes (Frehlich and Sharman 2008) and for the boundary layer (Lenschow and Sun 2007). However, the model results show considerable sensitivity to the model configuration (e.g., number of model levels and vertical grid spacing, PBL parameterization, depth and strength of the sponge layer, and terrain representation), and the influence of these and other model parameterizations has not been systemically evaluated.

In conclusion, results show that, although the WRF model with its mesoscale resolution cannot fully represent the small-scale variability observed in the high-rate thermosonde profiles, using second-order structure functions from the model to compute C_n^2 does capture a significant amount of the observed average signal without any particular bias and appears to provide accuracies that are at least competitive with more traditional models of C_n^2 that use measured or modeled vertical differences. Useful results were produced for both 10–12-h forecasts (1800 UTC initialization) and 16–18-h forecasts (1200 UTC initialization).

Acknowledgments. Some of this research was supported by the U. S. Army Test and Evaluation Command through an Interagency Agreement with the National Science Foundation. The thermosonde turbulence, temperature, relative humidity, and wind speed and direction data shown in Figs. 2, 3, 7, 8, and 9 are declared the work of the U.S. Government and are not subject to copyright protection in the United States. We thank Tom Warner for his review of an earlier version of this manuscript. We also thank the three anonymous reviewers for their careful reading of the manuscript and useful suggestions.

REFERENCES

Bufton, J. L., 1975: A radiosonde thermal sensor technique for measurement of atmospheric turbulence. NASA Tech. Note D-7867, 41 pp.

Cherubini, T., S. Businger, R. Lyman, and M. Chun, 2008: Modeling optical turbulence and seeing over Mauna Kea. *J. Appl. Meteor. Climatol.,* **47,** 1140–1155.

Cho, J. Y. N., and E. Lindborg, 2001: Horizontal velocity structure functions in the upper troposphere and lower stratosphere 1. Observations. *J. Geophys. Res.,* **106,** 10 223–10 232.

——, and Coauthors, 1999: Horizontal wavenumber spectra of winds, temperature, and trace gases during the Pacific Exploratory Missions: 1. Climatology. *J. Geophys. Res.,* **104,** 5697–5716.

Daley, R., 1993: Estimating observation error statistics for atmospheric data assimilation. *Ann. Geophys.,* **11,** 634–647.

Dewan, E. M., R. E. Good, R. Beland, and J. Brown, 1993: A model for C_n^2 (optical turbulence) profiles using radiosonde data. Environmental Research Paper 1121, PL-TR-93-2043, Phillips Laboratory, Hansom Air Force Base, 42 pp.

Doviak, R. J., and D. S. Zrnić, 1993: *Doppler Radar and Weather Observations*. Academic Press, 562 pp.

Ferziger, J. H., and M. Perić, 2002: *Computation Methods for Fluid Dynamics*. Springer-Verlag, 423 pp.

Frehlich, R. G., and R. Sharman, 2004: Estimates of turbulence from numerical weather prediction model output with applications to turbulence diagnosis and data assimilation. *Mon. Wea. Rev.,* **132,** 2308–2324.

——, and ——, 2008: The use of structure functions and spectra from numerical model output to determine effective model resolution. *Mon. Wea. Rev.,* **136,** 1537–1553.

Frehlich, R., Y. Meillier, M. L. Jensen, and B. Balsley, 2004: A statistical description of small-scale turbulence in the low-level nocturnal jet. *J. Atmos. Sci.,* **61,** 1079–1085.

Goody, R. M., 1964: *Atmospheric Radiation*. Clarendon Press, 436 pp.

Hong, S.-Y., Y. Noh, and J. Dudhia, 2006: A new vertical diffusion package with an explicit treatment of entrainment processes. *Mon. Wea. Rev.,* **134,** 2318–2341.

Hufnagel, R. E., 1978: Propagation through atmospheric turbulence. *The Infrared Handbook,* 2nd ed. W. L. Wolfe and G. J. Zissis, Eds., Office of Naval Research, 1–56.

Janjić, Z. I., 2002: Nonsingular implementation of the Mellor–Yamada level 2.5 scheme in the NCEP Meso model. NCEP Office Note 437, 61 pp.

Klemp, J. B., J. Dudhia, and A. D. Hassiotis, 2008: An upper gravity-wave absorbing layer for NWP applications. *Mon. Wea. Rev.,* **136,** 3987–4004.

Lenschow, D. H., and J. Sun, 2007: The spectral composition of fluxes and variances over land and sea out to the mesoscale. *Bound.-Layer Meteor.,* **125,** 63–84.

——, J. Mann, and L. Kristensen, 1994: How long is long enough when measuring fluxes and other turbulence statistics? *J. Atmos. Oceanic Technol.,* **11,** 661–673.

Lindborg, E., 1999: Can the atmospheric kinetic energy spectrum be explained by two-dimensional turbulence? *J. Fluid Mech.,* **388,** 259–288.

——, 2006: The energy cascade in a strongly stratified fluid. *J. Fluid Mech.,* **388,** 207–242.

Mahalov, A., and M. Moustaoui, 2010: Characterization of atmospheric optical turbulence for laser propagation. *Laser Photon. Rev.,* **4,** 144–159.

Mahrer, Y., 1984: An improved numerical approximation of the horizontal gradients in a terrain-following coordinate system. *Mon. Wea. Rev.,* **112,** 918–922.

Masciadri, E., J. Vernin, and P. Bougeault, 1999: 3D mapping of optical turbulence using an atmospheric numerical model. *Astron. Astrophys. Suppl. Ser.,* **137,** 185–202, doi:10.1051/aas:1999474.

Nastrom, G. D., and K. S. Gage, 1985: A climatology of atmospheric wavenumber spectra of wind and temperature observed by commercial aircraft. *J. Atmos. Sci.,* **42,** 950–960.

Papoulis, A., 1965: *Probability, Random Variables, and Stochastic Processes*. McGraw-Hill, 583 pp.

Press, W. H., B. P. Flannery, S. A. Teukolsky, and W. T. Vetterling, 1986: *Numerical Recipes: The Art of Scientific Computing*. Cambridge University Press, 963 pp.

Riley, J. J., and E. Lindborg, 2008: Stratified turbulence: A possible interpretation of some geophysical turbulence measurements. *J. Atmos. Sci.,* **65,** 2416–2424.

Skamarock, W. C., 2004: Evaluating mesoscale NWP models using kinetic energy spectra. *Mon. Wea. Rev.,* **132,** 3019–3032.

——, and Coauthors, 2008: A description of the Advanced Research WRF version 3. NCAR Tech. Note NCAR/TN-475+STR, 113 pp.

Tatarski, V. I., 1967: *Wave Propagation in a Turbulent Medium*. Dover, 285 pp.

Van Zandt, T. E., K. S. Gage, and J. M. Warnock, 1981: An improved model for the calculation of profiles of C_n^2 and ε in the free atmosphere from background profiles of wind, temperature and humidity. Preprints, *20th Conf. on Radar Meteorology,* Boston, MA, Amer. Meteor. Soc., 129–135.